Activation of Prussian blue analogues:
Temperature effects on structure, porosity, and open metal site accessibility

Albertsma, J.; Koopman, C.I.; Draaijer, G.D.; Rook, W.; Vermaas, D.A.

DOI
10.1016/j.micromeso.2025.113959

Publication date
402

Document Version
Final published version

Published in
Microporous and Mesoporous Materials

Microporous and Mesoporous Materials 402 (2026) 113959

Contents lists available at ScienceDirect

Microporous and Mesoporous Materials

journal homepage: www.elsevier.com/locate/micromeso

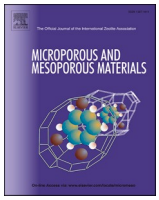

Activation of Prussian blue analogues: Temperature effects on structure, porosity, and open metal site accessibility

Jelco Albertsma, Christel I. Koopman, Eise Draaijer, Willy Rook, David A. Vermaas, Monique A. van der Veen *

Department of Chemical Engineering, Delft University of Technology, Van der Maasweg 9, 2629 HZ, Delft, the Netherlands

ARTICLE INFO

Keywords:
Prussian blue analogues
Activation
Adsorption
Gas separation

ABSTRACT

Prussian blue analogues (PBAs) are low-cost porous materials with promising potential in gas separation, owing to their abundance of open metal sites. To access these open metal sites PBAs need to be activated through removal of water from the porous structure. However, the conditions required for effective activation and their structural consequences remain poorly understood, with existing effective methods being costly. Therefore, to gain insights in the activation process and its effects on structure, we systematically investigated the effect of activation temperature on three different ferricyanide-based PBAs (FePBA, CoPBA, and CuPBA) using a simple nitrogen flow activation procedure. We successfully synthesised these structures and optimised the activation procedure for micropore capacity and crystallinity. Infrared spectroscopy as well as CO_2 and CO adsorption measurements revealed that, even under optimised conditions, water remained within the PBAs, with only a limited number of open metal sites accessible. At higher activation temperatures, micropore capacity and crystallinity decrease. This hydrophilicity, however, also showed positives, for example in the application of PBAs as desiccants. CuPBA, specifically, boasts a water adsorption of 355 mg g^{-1} at a relative humidity of $\leq$10%, competitive with zeolites and silica per weight unit, but higher per volume unit. Overall, however, while PBAs offer promise for gas adsorption owing to their high surface area and low cost, practical utilisation of their open metal sites remains challenging due to their strong affinity for water.

1. Introduction

Due to the increasing population and wealth levels in the world, more and more resources are expended, resulting in more emissions of industrial waste gases [1,2]. Polluting and useful chemicals should be separated out of these waste gas streams in order to achieve a cleaner environment and better resource utilisation. In view of climate goals, this separation should have a low energy consumption as well as a high selectivity for the target chemicals. One such a separation technique for gas separations, which has the potential to be used as a lower energy cost alternative to cryogenic distillation, is adsorption [3]. Adsorption has the additional advantage of having a large library of porous materials available such as porous carbons [4], zeolites [5], metal-organics frameworks [6], etc. This range of materials allows for the targeting of specific properties and material features to obtain a more selective separation. Coordinatively unsaturated metal sites, also called open metal sites, are such a feature which can adsorb many of the typical gases in waste streams: CO_2 [7], CO [8], NO_x [9], etc., due to their strong interactions.

One class of materials that can contain open metal sites are Prussian blue analogues (PBAs). PBAs are coordination polymers consisting of transition metal cations and metal cyanide anions with structures similar to the eponymous pigment [10,11] with the generalised chemical formula of $C_xM1[M2(CN)_6]_{1-y}\cdot\Diamond_y\cdot wH_2O$ [12–14]. In this formula C_x indicates alkali metal ions, M1 indicates transition metal cations, $[M2(CN)_6]^{n-}_{1-y}$ are the hexacyanometallate anions, $\Diamond_y$ are the hexacyanometallate vacancies, and wH_2O are the water molecules in the PBA. We will generally refer to the PBA structures in this paper by the shortened $M1[M2(CN)_6]_{1-y}\cdot\Diamond_y$ notation for easier legibility.

By choosing the correct ratios and oxidation states of the reactants, insoluble microporous PBAs can be produced [11] which have a network of linked voids created by $M(CN)_6$vacancies (Fig. 1) [14]. Other than porosity, having these vacancies is additionally advantageous due to the maximum of 6 open metal sites that are created per vacancy. This

* Corresponding author.
E-mail address: m.a.vanderveen@tudelft.nl (M.A. van der Veen).

https://doi.org/10.1016/j.micromeso.2025.113959
Received 17 September 2025; Received in revised form 20 November 2025; Accepted 21 November 2025
Available online 22 November 2025

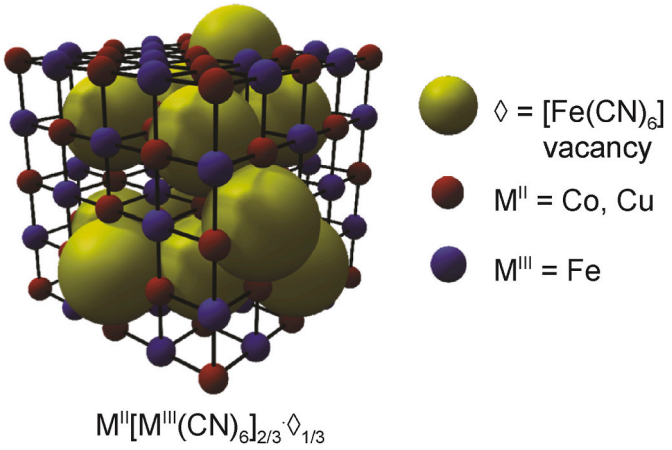

Fig. 1. Schematic image of $M^{II}[Fe^{III}(CN)_6]_{2/3}\cdot\Diamond_{1/3}$ PBAs based on ref. [14].

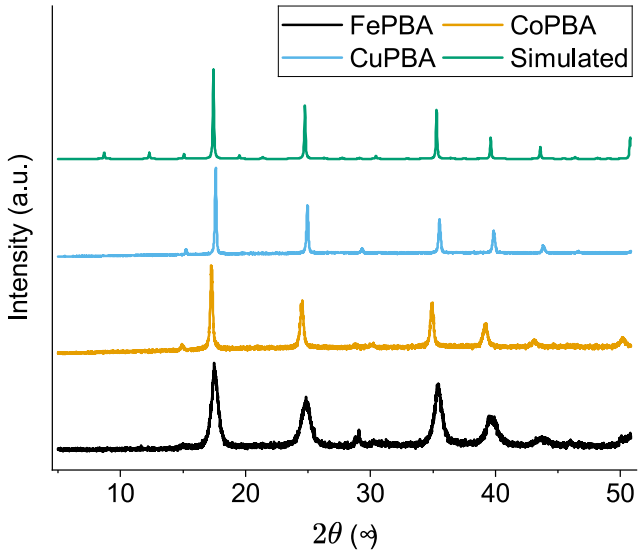

Fig. 2. Normalised PXRDs of the as-synthesised PBAs compared to a simulated pattern. The simulated pattern is reproduced using single crystal data of Prussian Blue from ref. [32]. (For interpretation of the references to colour in this figure legend, the reader is referred to the Web version of this article.)

amounts to a theoretical open metal concentration of up to 1 per formula unit ($M1^{II}[M2^{III}(CN)_6]_{2/3}\cdot\Diamond_{1/3}$) or 5 mmol g^{-1} which is similar to the highest concentrations found in typical metal-organic frameworks [15] and higher than found in metal-exchanged zeolites [16]. Another advantage of PBAs compared to other tailorable porous solids is that they can be made from very abundant materials through a facile aqueous precipitation reaction [10,11,17,18]. This makes PBAs promising for large-scale, industrial applications.

PBAs with their abundant open metal sites do have one major drawback, however, which is the potential inaccessibility of these sites due to the presence of coordinated water. Water is known to interact strongly with open metal sites [19,20] and microporous materials are known to retain water due to capillary effects [21,22]. Water, thus, competitively adsorbs on the same open metal sites as desired target molecules from waste gas streams [8,9,23]. This means that the presence of humidity will negatively affect the adsorptive separation on PBAs. Moreover, water will already be present from the synthesis which means activation, i.e., the removal of water from the pores, is an important aspect in the feasibility of utilising the open metal sites in PBAs.

Previous research on gas adsorption in PBAs has shown that obtaining accessible open metal sites is possible by using high vacuum with long degassing times (≥24 h) while strenuously keeping the PBAs isolated from the atmosphere [17,24] In many other cases, however, little attention is paid to whether the activation procedure fully removes water and whether the structure is retained after activation [18,25–28]. Another issue is that the aforementioned successful activation procedure is often unviable for large scale applications due to the required high vacuum and long degassing times. Therefore, we investigated whether microporous PBAs could be activated while optimising their micropore structure using a simple sub-24 h N_2-based activation procedure. This research aims to provide insight into the feasibility of accessing open metal sites in PBAs, while taking into account effects on the structure due to the removal of water.

We chose to perform this research using $[Fe(CN)_6]^{3-}$-ions, as this is the cheapest and most readily available $[M2^{III}(CN)_6]^{3-}$-ion, to create $M1^{II}[M2^{III}(CN)_6]_{2/3}\cdot\Diamond_{1/3}$ PBAs with inherent microporosity. As the other metal ($M1^{II}$) in these PBAs, we chose Fe^{2+}, Co^{2+}, and Cu^{2+} as these are transition metals which lead to interesting structural characteristics in PBAs. Co should lead to the prototypical $M1^{II}[M2^{III}(CN)_6]_{2/3}\cdot\Diamond_{1/3}$ PBA with a space group of $Fm\bar{3}m$, which will serve as a baseline to the other PBAs. Cu is interesting due to Cu-based PBAs having the highest reported storage capacity for H_2 compared to other PBAs [25]. Unlike the other two structures, Fe will not show an inherent pore network such as shown in Fig. 1. This is caused by the difference in the most stable oxidation state between the dissolved ions (Fe^{2+} and $Fe(CN)_6^{3-}$) and the solid PBA (Fe^{3+} and $Fe(CN)_6^{4-}$). In the end, this change in oxidation states of the individual ions, which create the PBA, leads to a $Fe^{III}[Fe^{II}(CN)_6]_{3/4}\cdot\Diamond_{1/4}$ PBA [14,29], in which only structural defects, rather than the inherent charge-balancing $[Fe(CN)_6]^{3-}$-vacancies that can be found in $M1^{II}[M2^{III}(CN)_6]_{2/3}\cdot\Diamond_{1/3}$ structures, lead to an extended micropore network [14]. The Fe-based PBA is interesting as a general comparison to the Co- and Cu-based PBAs, but it also shows if our methodology is more generally applicable.

2. Experimental section

2.1. Materials

$FeSO_4\cdot 7H_2O$ (≥99%), $CoSO_4\cdot 7H_2O$ (≥99%), $CuSO_4\cdot 5H_2O$ (≥98.0%), and $K_3[Fe(CN)_6]$ (≥99%) were purchased from Sigma-Aldrich and used without further purification.

2.2. Synthesis of PBAs

MPBAs ($M^{II}[Fe^{III}(CN)_6]_{2/3}\cdot\Diamond_{1/3}$, M = Co, Cu and $Fe^{III}[Fe^{II}(CN)_6]_{3/4}\cdot\Diamond_{1/4}$, $\Diamond = [Fe^{III}(CN)_6]^{n-}$ vacancy with n = 4 for Fe and 3 for Co and Cu-based PBAs) were synthesised by dropwise addition of $K_3[Fe(CN)_6]$ (8.231 g, 25 mmol, 1 equiv.) dissolved in 250 ml of demiwater, into $MSO_4\cdot xH_2O$ (75 mmol, 3 equiv.) in 250 ml of demiwater at 50 °C under stirring. After complete addition of the $K_3[Fe(CN)_6]$-solution, the mixture was left to stir at 50 °C for another 2 h. The resulting solids were separated by centrifugation (4000 RCF, 5 min) and washed with fresh demiwater 3 times by redispersing and centrifuging. The solids were then dried in a vacuum oven at 60 °C until dry.

2.3. Methods

Powder X-ray Diffraction (PXRD) was performed on a Bruker Advance D8 with a Cu K_α source and a Ni monochromator.

Elemental composition was determined by Mikroanalytisches Laboratorium Kolbe, Germany. C, H, and N were determined using an Elementar Model Vario Mikro CHNS analyser. Fe, Cu, Co, and K were determined by a Spectro Model Spectro Acros ICP after microwave digestion in a CEM MARS 6.

Degassing for N_2, CO_2, and CO adsorption was performed on a

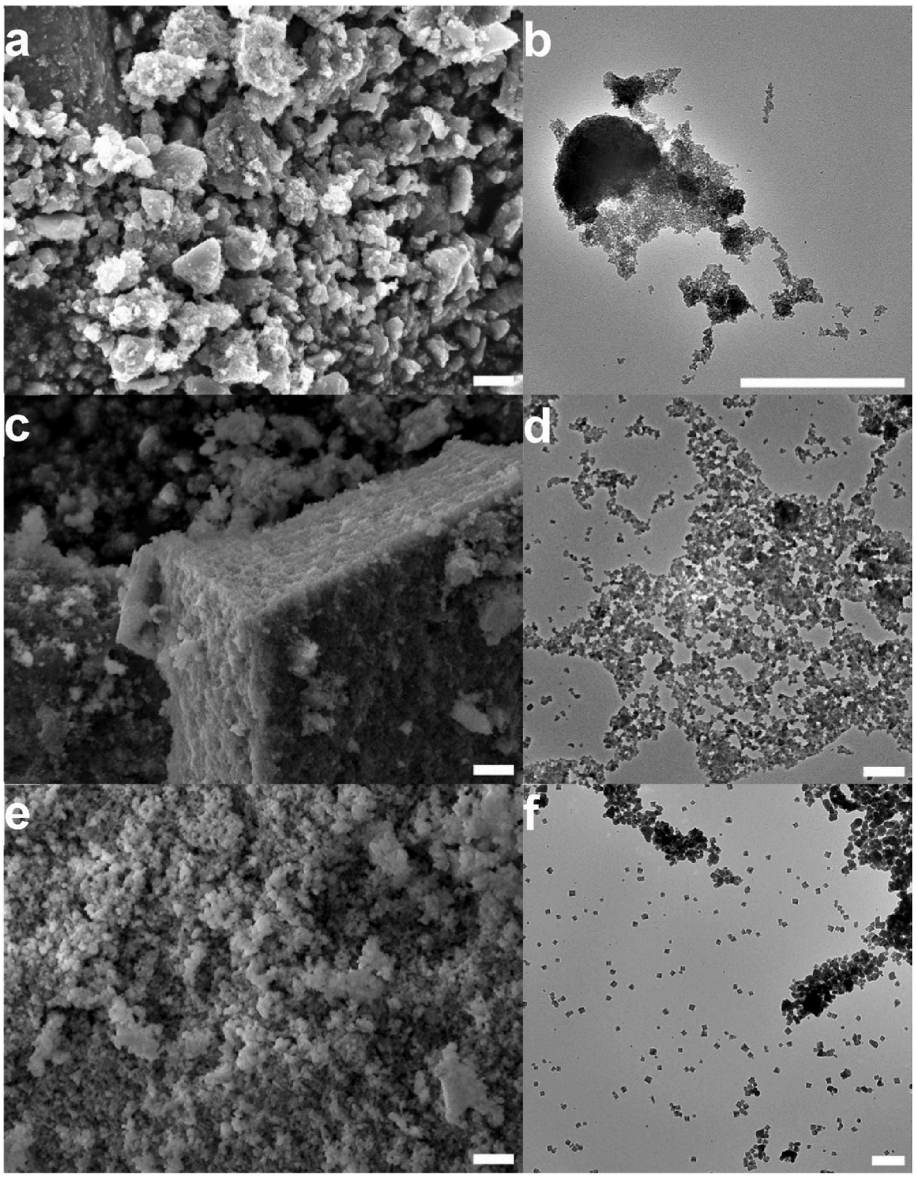

Fig. 3. SEM and TEM images of as-synthesised FePBA (a,b), CoPBA (c,d), and CuPBA (e,f). The scale bar is 1 μm and 500 nm for the SEM and TEM images, respectively.

Micromeritics SmartPrep with a heating rate of 5 °C min^{-1} under a flow of N_2. Degassing was done for 15 h at various temperatures for the N_2 adsorption of the PBA samples to investigate temperature effects on the degassing: FePBA (60, 90, 100, 110, 120, 140 °C), CoPBA (60, 90, 100, 110, 120, 140 °C), and CuPBA (60, 100, 110, 120, 130, 140 °C). In case the degassing temperature was 90 °C or higher, a pre-drying step was performed at 90 °C for 1 h before the final degassing temperature to prevent samples from being damaged by rapid evaporation of water in the pores. Degassing for CO_2, CO, and H_2O adsorption were done at the optimal temperatures as determined by N_2 adsorption (FePBA, 100 °C; CoPBA, 100 °C; CuPBA, 120 C). Due to the high vacuum under which water adsorption is performed, these samples were additionally degassed under vacuum in a Micromeritics VacPrep for 1 h at their optimal temperature and overnight thereafter at 25 °C.

N_2 and CO_2 adsorption isotherms were measured on a Micromeritics TriStar II at 77 K and 298 K, respectively. H_2O adsorption isotherms were obtained on a Micromeritics 3Flex at 293 K. CO adsorption was performed on a Micromeritics ASAP 2020C at 303 K. Sample size for N_2, CO_2, and H_2O adsorption was around 150 mg before degassing, while a larger sample of ≥350 mg was used for CO adsorption. BET values were calculated from the N_2 adsorption data for the optimally degassed samples according to the Rouquerol criteria [30] in the BETSI programme [31].

DRIFTS was measured on a Thermo Nicolet Nexus FT-IR equipped with a Harrick Praying Mantis and a high temperature reaction chamber with ZnSe windows. All DRIFTS measurements were performed at 25 °C with a flow of 30 mL min^{-1} N_2 against a KBr background measured under the same conditions. The in-situ drying followed the same procedure as was used for the degassing for the N_2 adsorption. Under the aforementioned N_2 flow, the samples were heated to 90 °C for 1 h with a heating rate of 5 °C min^{-1}, after which they were heated with a heating rate of 5 °C min^{-1} to their optimum temperature (FePBA, 100 °C; CoPBA, 100 °C; CuPBA, 120 °C) which was kept for 15 h and then left to naturally cool to 25 °C.

SEM measurements were performed using a JEOL JSM-IT700HR.

TEM measurements were performed in a JEOL TEM-1400Plus electron microscope using Cu-supported continuous carbon grids.

Thermogravimetric analysis (TGA) was performed on a Mettler Toledo TGA/SDTA851e under 100 mL min^{-1} of N_2 with an isothermal step at 30 °C for 10 min followed by a heating step with a rate of 1 °C

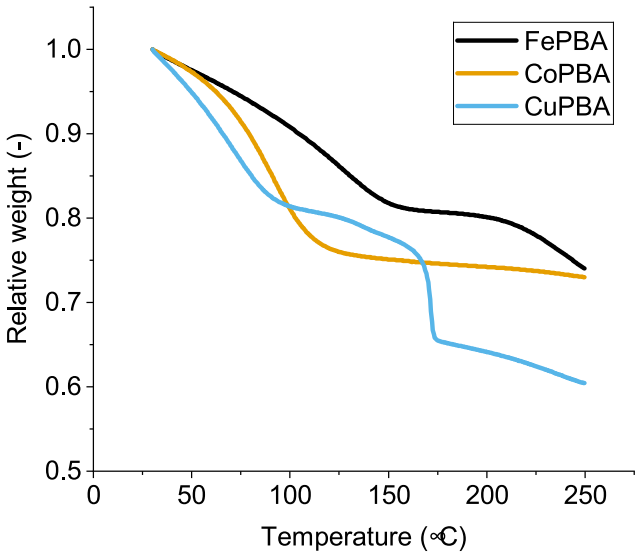

Fig. 4. Thermogravimetric analysis of PBA samples, 1 °C min^{-1} under 100 mL min^{-1} N^2.

min^{-1} from 30 to 250 °C.

3. Results and discussion

Fig. 2 shows the results of the synthesis of the FePBA, CoPBA, and CuPBA. It is clear that all PBAs show the same overall structure as Prussian blue, as the major peaks at 17.5, 25, 36, 40 and 44° match that of the simulated 3 pattern. Both CoPBA and CuPBA show a high degree of crystallinity with well-defined peaks without much broadening. FePBA, on the other hand, does show significant amounts of broadening which is indicative of a smaller crystallite size compared to the CoPBA and CuPBA and might be caused by a more defective $Fe^{III}_4[Fe^{II}(CN)_6]_3$ structure rather than a $M^{II}[Fe^{III}(CN)_6]_{2/3}\cdot\Diamond_{1/3}$ structure due to the suboptimal reactant stoichiometry and oxidation states for this structure [29].

The SEM analysis of the as-synthesised particles (Fig. 3a, c, and e) shows that the synthesised PBAs all show relatively anhedral particles which clump together in larger aggregates. The TEM measurements (Fig. 3b, d, and f) confirm that in FePBA and CoPBA the particles are all amorphous, while CuPBA has a mixture of anhedral and cubic particles which was not visible in the SEM results. The TEM images also show that the particle size of FePBA is much smaller than the similarly sized CoPBA and CuPBA particles, which is in agreement with the results of the PXRD.

The elemental composition is similar to the expected values (Table S1). In terms of atomic ratios this can be translated to: FePBA (C:H:N:Fe:K, measured 1:2.30:0.96:0.35:0.03, expected 1:0:1:0.39:0 from $Fe_4[Fe(CN)_6]_3$), CoPBA (C:H:N:Fe:Co:K, measured 1:2.33:1.04:0.16:0.24:0.01, expected 1:0:1:0.17:0.24:0 from $Co_3[Fe(CN)_6]_2$), CuPBA (C:H:N:Fe:Cu:K, measured 1:2.33:1.04:0.17:0.20:0, expected 1:0:1:0.17:0.25:0 from $Cu_3[Fe(CN)_6]_2$). While the ratios of the expected elements are largely close to the expected values, there is also H and K present. The H content can simply be attributed to the presence of water, while K comes from K^+-ions which are known to potentially intercalate in the PBA structure. However, the K^+ concentrations are small and we do not expect major effects on the overall results.

The thermogravimetric analysis (Fig. 4) shows a typical decrease in relative weight with some plateaus at which weight loss is minimal. These plateaus appear at around 150, 110, and 90 °C for FePBA, CoPBA, and CuPBA, respectively, with weight losses between 15 and 25%. However, the plateaus are relatively sloped and choosing a degassing temperature purely based on the TGA still leaves uncertainty on the removal of water and the structural stability of the PBAs. Hence, we chose to systematically vary the degassing temperature to obtain the highest microporosity. After the degassing, N_2 adsorption and PXRD were performed to observe degassing related changes in the structures (Fig. 5 and Table S2).

The N_2 sorption isotherms of FePBA (Fig. 5a) show a sharp increase in adsorbed N_2 at a relative pressure below 0.1 and a clear continuous increase with relative N_2 pressure beyond that point up to a relative pressure of 0.8. A clear hysteris is also visible in the desorption part of the measurement between a relative pressure of 0.9 to 0.4. These observations in the isotherms are indicative of clear mesoporosity with some microporosity. The mesopore capacity stays constant for activation temperatures up to 100 °C as can be seen in the constant slope of the isotherm between 0.1 and 0.8 relative pressure. Above 100 °C, on the other hand, the mesopore capacity starts to increase as seen by the increasing slope in the adsorption isotherm between 0.1 and 0.8 relative pressure. $cm^3\ g^{-1}$ STP using a degassing of 60 °C to 64 $cm^3\ g^{-1}$ STP at 100 °C (see Table S2 for values and methodology), after which it again decreases. This leads to an overall capacity that increases between 60 °C and 100 °C from 120 to 145 $cm^3\ g^{-1}$ STP. Degassing temperatures above 100 °C cause an overall loss of capacity due to a higher decrease in micropore capacity than the gain in mesopore capacity until these effects equal at about 120 °C. Above 120 °C, the overall capacity then increases again due to the dominant effects from the increasing mesopore capacity, resulting in a maximum adsorption capacity of 150 $cm^3\ g^{-1}$ STP. If we compare the results from the N_2 adsorption with the PXRD (Fig. 5d), we can see that the overall structure of the FePBA is retained. While there are some small changes in the peak intensities and FWHM values (Table S3), no clear structural degradation is visible.

CoPBA (Fig. 5b, e), on the other hand, has a largely microporous structure with limited mesoporosity which can be seen by the sharp increase in adsorbed N_2 at $P/P_0 < 0.1$ and the slight slope in the isotherm between a relative pressure of 0.1 and 0.8, respectively. The micropore volume lies around 150 $cm^3\ g^{-1}$ STP which is stable within about 15 $cm^3\ g^{-1}$ STP over the temperature range of degassing. The sharp increase in adsorption at $P/P_0 \geq 0.8$ can be attributed to N_2 condensating in the narrow voids between nanoparticles (Fig. 3c and d). The maximum micropore capacity, while maintaining framework crystallinity, is achieved at a degassing temperature of 100 °C. Unlike FePBA, no mesopores are generated at higher degassing temperatures; instead, micropore capacity decreases above 100 °C. Crystallinity is preserved up to 100 °C, as evidenced by the intensity and sharpness of the PXRD peaks. Beyond this temperature, a slight reduction in peak intensity and an increase in FWHM (Table S3) are observed, indicating a progressive loss of crystallinity. These results suggest that degassing temperatures exceeding 100 °C begin to degrade the framework structure.

Similarly to CoPBA, CuPBA (Fig. 5c, f) shows mostly microporosity as can be seen by the sharp increase in adsorbed N_2 at $P/P_0 < 0.1$ with a similar, albeit smaller, increase in adsorption due to condensation of adsorbate between small particles (Fig. 3e and f) at $P/P_0 \geq 0.8$. Unlike in CoPBA, however, there is a strong effect of the degassing temperature on the porosity of CuPBA. The micropore volume increases from 57 $cm^3\ g^{-1}$ STP using a degassing temperature of 60 °C to a maximum of 211 $cm^3\ g^{-1}$ STP at a degassing temperature of 120 °C. Above that temperature, however, the structure completely collapses which is indicated by both the almost complete loss of N_2 adsorption and the loss of crystallinity in the PXRD at degassing temperatures of 130 C and above. At a degassing temperature of 120 °C and below, the overall crystallinity is well-maintained with some small variations in peak intensity and FWHM values (Table S3). These crystallographic changes are, however, not accompanied by significant morphological changes as can be observed in the TEM analysis after degassing (Figure S8 and S9).

We conclude that the optimal degassing procedures to obtain the highest micropore capacity for FePBA, CoPBA, and CuPBA are at 100 °C, 100 °C, and 120 °C, respectively, with BET values of 271, 635, and 890 $m^2\ g^{-1}$ (Figs. S1–S4 and Table S4). If this corresponds to successful water

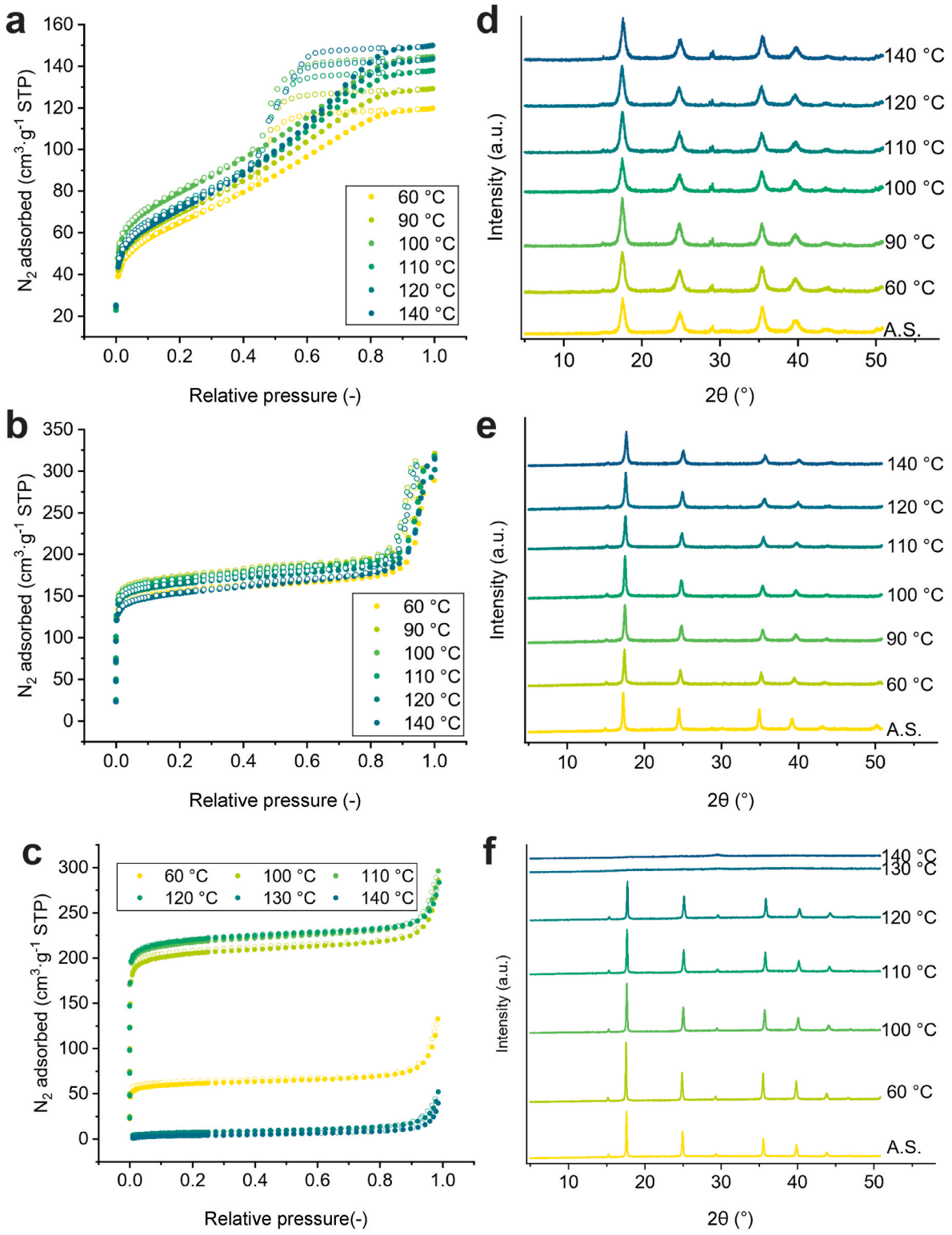

Fig. 5. N_2 adsorption at 77 K and PXRD results of FePBA (a,d), CoPBA (b,e), and CuPBA (c,f). Temperature in the figures indicates the degassing temperature. Closed and open symbols indicate the adsorption and desorption branches of the isotherm, respectively.

removal from the open metal sites, a strong interaction with CO_2 should ensue [33,34].

Fig. 6 shows the CO_2 adsorption isotherms for the three PBA's activated at the optimal temperatures. The uptake at 120 kPa lies at 1.6, 1.8, and 2.6 mmol g^{-1} for FePBA, CoPBA, and CuPBA, respectively, which is substantial. However, the Henry coefficient around 0.03 mmol g^{-1} kPa^{-1} for the initial uptake is rather modest, indicating the lack of strong interaction between CO_2 and the PBA, indicative of a lack of available open metal sites. The significant CO_2 adsorption at high partial pressure is likely physisorption of CO_2 via van der Waals interactions with the small micropores. Indeed the trend in total uptake at 120 kPa (CuPBA > CoPBA > FePBA) also corresponds to the trend in micropore volume (see Fig. 3a–c). This serves as a first indication that we have not fully removed water from the open metal sites.

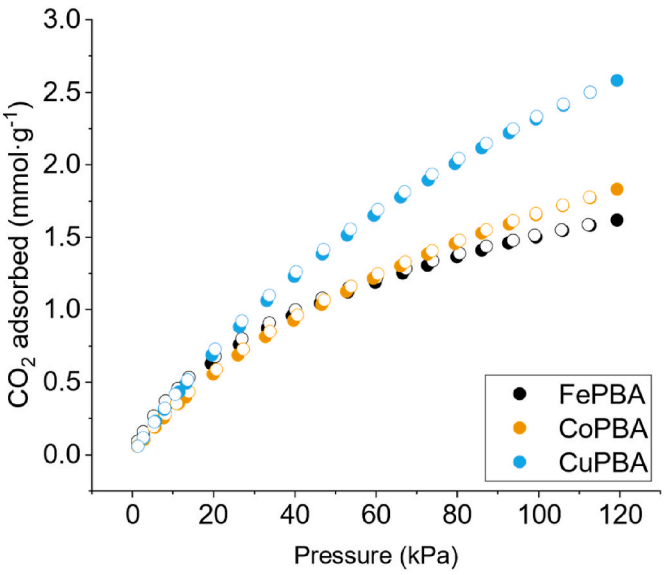

Fig. 6. CO_2 adsorption at 298 K on the PBAs after the optimal degassing procedure. Closed and open symbols indicate the adsorption and desorption branches of the isotherm, respectively.

In addition, water removal was assessed in-situ via DRIFTS measurements during the activation procedure at the optimised temperatures (see Methods). Fig. 7 shows the large spectral features associated with water, such as the peak at 3700 cm^{-1} (non-hydrogen bonded O-H stretch vibration), the broad peaks at 3500-2750 cm^{-1} (hydrogen bonded O-H stretch vibration), and the peaks around 1600 cm^{-1} (H-O-H bending vibrations), in all PBAs before the drying procedure. After the in-situ drying procedure, the intensity of these signals decreases strongly, indicating the removal of water. However, in all cases water signals in the region of 3700 cm^{-1} to 2275 cm^{-1} are still clearly present in the spectra, indicating that while a substantial amount of the bulk water was removed, complete removal was not achieved using the drying procedure. Even when using degassing temperatures above the point where each respective PBA starts structurally deteriorating, water-related IR signals can still be seen in the DRIFTS graph, indicating that the N_2-based degassing method will not fully remove water even at higher temperatures (Figs. S5–S7: XRD, N_2-sorption and FTIR spectra for FePBA and CoPBA activated at 220 °C and CuPBA at 130 °C).

As a final measurement to conclude whether some of the open metal sites can still be accessed, physisorption and chemisorption of CO was measured, since CO is known to interact with many open metal sites, potentially competitively, in the presence of water. Moreover, if the PBAs are capable of selectively adsorbing CO it will be of interest in the usage for the CO/N_2 separation for which there is no industrially relevant method yet [8]. The CO adsorption measurement consists of two consecutive adsorption isotherm measurements per sample. The first one is performed after degassing at the optimised temperature. After this measurement, vacuum is applied for 1 h at the measurement temperature to desorb physisorbed CO, but not chemisorbed CO. After this vacuum treatment a second adsorption measurement is started. This results in two isotherm lines, the difference between which is presumed to be the chemisorption part of the total adsorption, while the second adsorption isotherm is presumed to be the physisorption part.

Fig. 8 shows the results of the CO adsorption measurements. The overall adsorption from the first measurement at 120 kPa by CuPBA is on the same order of magnitude as the best performing CO adsorbents known [8] at 1.24 mmol g^{-1}, while CoPBA and FePBA adsorb a more modest 0.43 and 0.26 mmol g^{-1}, respectively. Similarly to the CO_2 adsorption, the overall CO adsorption follows the trend of micropore capacity (CuPBA > CoPBA > FePBA) with no strong adsorption visible in terms of Henry coefficient of 0.005, 0.01, and 0.02 mmol g^{-1} kPa^{-1} for FePBA, CoPBA, and CuPBA, respectively. When looking at the differences between the first and second CO adsorption measurement, interesting observations can be made. In the case of FePBA and CoPBA, a significant, constant difference between the first and repeat measurements can be seen, indicating 0.08 and 0.02 mmol g^{-1} of chemisorption as well as 0.40 and 0.18 mmol g^{-1} of physisorption at 120 kPa, for FePBA and CoPBA, respectively. For CuPBA, we observe differences between the two measurements which are not consistent across the pressure range. We can see a higher initial increase in CO uptake at low pressures (<45 kPa) in the second measurement compared to the first. After this point we see a lower uptake in the second measurement compared to the first one. We presume this phenomenon occurred due to the vacuum step between the two measurements, in which additional adsorbed gases are removed. We hypothesise that this 1 h high-vacuum step removed some of the bound water leading to the increase at low pressures, while more strongly bound CO that remains after the vacuum step leads to the overall lower adsorption at higher pressures. If we assume that the difference at 120 kPa is the overall chemisorption, that would mean a value of 0.09 mmol g^{-1} of chemisorption and 1.15 mmol g^{-1} of physisorption at 120 kPa.

If we compare the chemisorptive adsorption values with the expected amount of open metal sites, we can see that there is a large difference. Experimentally, we observe chemisorption values of 0.02, 0.08, and 0.09 mmol g^{-1} for CoPBA, FePBA, and CuPBA, respectively. Theoretically, however, we expect to see 6 open metal sites per $[Fe(CN)_6]^{3-}$ removed from the structure for a perfect $(M1^{II}[M2^{III}(CN)_6]_{2/3} \cdot \Diamond_{1/3})$ crystal. This translates to 1 open metal site per formula unit, which is equal to about 5 mmol open metal site per gram of PBA. Not all open metal sites, however, would necessarily chemisorb CO. Previous work has shown a strong interaction between Co^{2+}-sites and CO through IR and CO adsorption studies [35]. Fe^{3+} and Cu^{2+} ions, on the other hand, generally do not have such strong interactions with CO even though significant physisorption can still occur [8]. However, due to the electron donating presence of the N-side of the CN^- ligands we expect a reduced effective charge on these metal ions, which may help strengthen the metal-CO interaction [25,36], potentially leading to a strong enough binding to be observed through our CO adsorption measurement. Nevertheless, the large difference between the measured and theoretical maximum CO adsorption indicates that only a small percentage of the total open metal sites was successfully activated and water-free. This result shows that water cannot be fully removed through a simple N_2-based activation procedure, and that the degree to which CO can competitively adsorb in the presence of water is very limited.

The water adsorption isotherms of the different PBAs are shown in Fig. 9. The overall uptake at a relative pressure of 1 is about 22, 35, and 25 mmol g^{-1} for FePBA, CoPBA, and CuPBA, respectively. In all cases, we can see a sharp, large uptake of water at very low relative pressures (<0.05), indicating that in addition to water adsorbed on open metal sites, water condensation into the micropores already occurs at very low humidity levels. We can also see some additional uptake between a relative pressure of 0.05 and 0.9 with some hysteresis in the desorption curve, which is most prominent in FePBA. This is in line with the higher mesopore capacity of FePBA: for increasingly larger mesopores condensation is expected at increasingly high relative humidity [37]. All tested PBAs exhibit pronounced hydrophilicity, as evidenced by the sharp uptake of water at low relative pressure. Comparison of the N_2 and water isotherms highlights this behaviour. The N_2 isotherms yield micropore volumes of 0.099, 0.248, and 0.327 mL g^{-1} for FePBA, CoPBA, and CuPBA, respectively (Table S2). In contrast, the water isotherms at a relative pressure of 0.1 show adsorption values of 10.8, 15.8, and 18.5 mmol g^{-1}, corresponding to 0.195, 0.286, and 0.334 g g^{-1} for FePBA, CoPBA, and CuPBA, respectively. These results demonstrate that at a relative pressure of 0.1 (10% relative humidity), the micropores are already saturated with water. Consequently, even under optimal activation, PBAs are unsuitable for gas adsorption in humid environments,

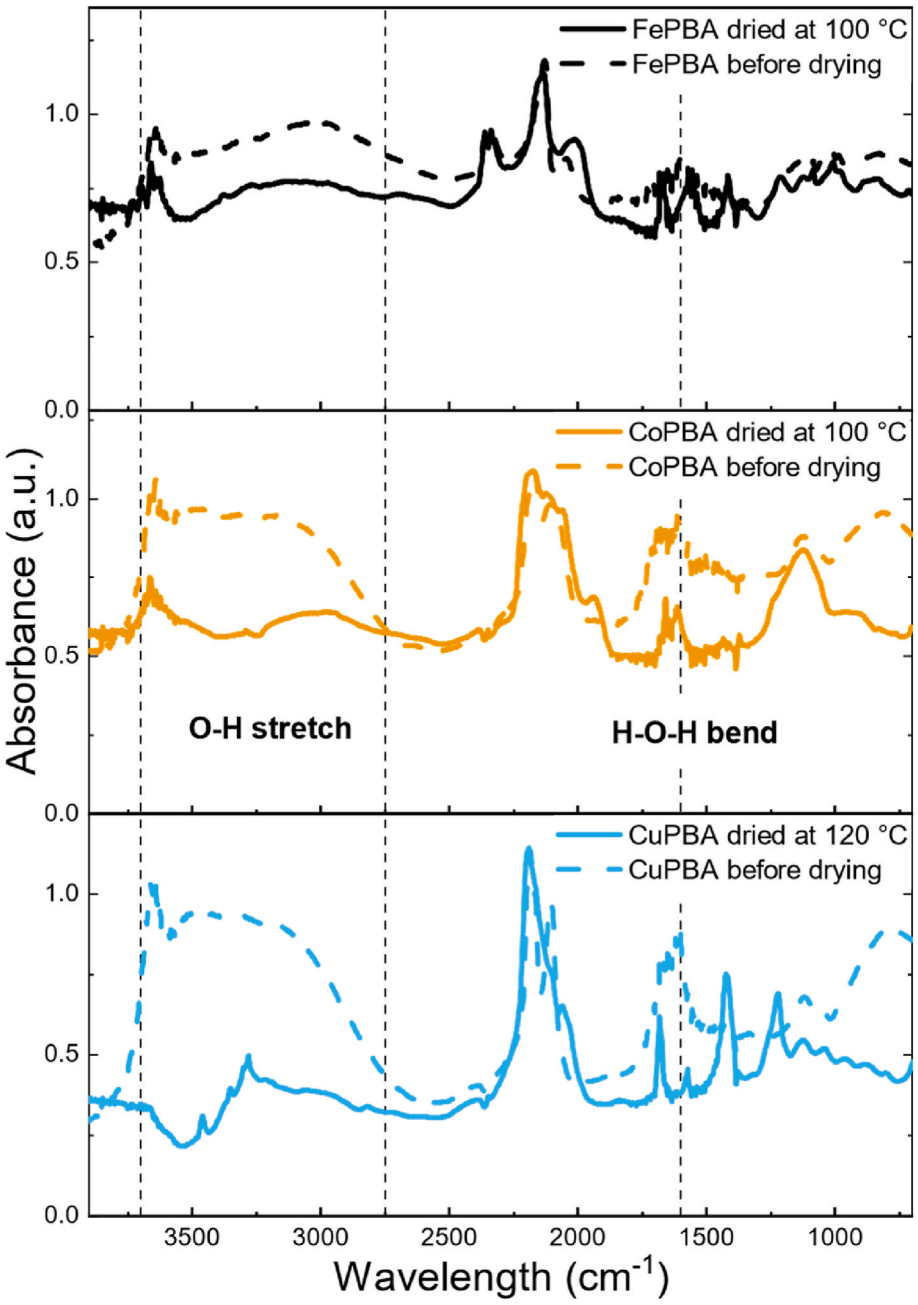

Fig. 7. DRIFTS measurements of the PBAs before and after the in-situ drying procedure.

as water condensation rapidly renders the micropore space inaccessible to other molecules. Notably, the water uptake of PBAs is comparable to that of high-performing zeolites used for drying applications, which typically adsorb around 0.4 g g^{-1} [38]. CuPBA exhibits a water adsorption capacity of 0.335 g g^{-1} at a relative pressure of 0.1. Given the lower volume per mass of PBAs compared to zeolites, PBAs warrant further evaluation as candidate materials for drying applications where compact volumes are advantageous.

4. Discussion

Through a set of experiments such as CO_2 and CO adsorption, we have shown that we are only able to obtain a small amount of open metal sites in the PBAs via a N_2 flow based degassing procedure. Through DRIFTS with in-situ degassing we were also able to conclude that there is still a significant amount of water present in the samples after degassing.

Comparing our results with literature on adsorption in PBAs, we can see that activation in these materials is indeed not a trivial matter. Only the research done by the Long group on $Cu[Co(CN)_6]_{2/3}\cdot\Diamond_{1/3}$ is conclusive on the removal of water and the retention of the structure, as well as the location of the adsorption sites for H_2 gas [17,24]. To obtain these results, however, a degassing procedure of 48 h under high vacuum with vacuum transfer steps was required.

These requirements are contrary to other adsorptive materials with open metal sites such as MOFs or zeolites. While the open metal sites in those materials are still highly hydrophilic and contact with water should be avoided, the actual degassing can be done using a N_2 flow method similar to the one we employed due to their better thermal stability which allows higher degassing temperatures [5,39].

Investigations on gas adsorption in PBAs showcase a general lack of attention paid to the effects of degassing on the structures of PBAs. For example, degassing temperatures are chosen without showing

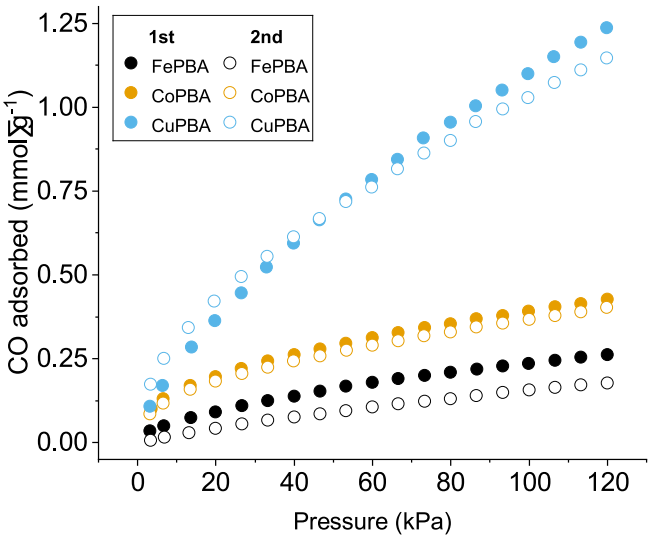

Fig. 8. CO adsorption at 303 K in chemisorption mode after the optimal degassing procedure.

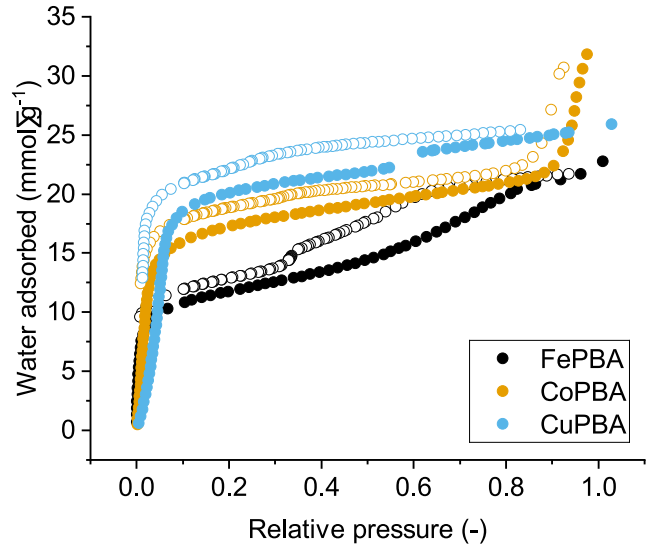

Fig. 9. Water adsorption at 293 K of the optimally degassed PBAs. Closed and open symbols indicate the adsorption and desorption branches, respectively.

verification of the complete removal of water [18,25–27]. Sometimes, multiple temperatures are used for seemingly similar materials for unexplained reasons [18,25,27]. In a similar vein, material properties after activation using techniques such as IR or XRD are often not reported [17,18], and generally the complete removal of water is assumed through the outgas rate [17,18,25] which is the rate at which gases are coming off the sample under vacuum. However, this is not a truly conclusive metric since it only accounts for weakly bound water and not necessarily for strongly bound water. Similarly, the outgas rate does not indicate whether structural degradation takes place.

These assumptions about activation can then lead to unexpected behaviour and underestimated adsorption compared to full activation. One example is the physisorption of CO_2 [26] in PBAs rather than the expected chemisorption when open metal sites are water-free [33,34]. This is similar to what we observed in our CO_2 adsorption experiments when water was still present on the metal sites (Fig. 6). In some other adsorption applications such as the adsorption of NH_3, the presence of water is not as noticeable since NH_3 can react with water into NH_4OH which masks incomplete activation [27,28]. Lastly, the effect of degassing on the structure, if reported in the first place, is typically only done through XRD comparison with the as-synthesised material [27,28] or is done to show chemical stability rather than thermal stability [26,27]. However, these tests do not capture the full effect of the degassing temperature on the porosity which we can show through our investigation combining XRD and N_2 adsorption (Fig. 5).

Our results, therefore, indeed indicate that, depending on the evacuation conditions, reduction in crystallinity and micropore capacity as well as incomplete water removal might be a regular occurrence in PBA-related research. This observation points to a general need to better describe i) degassing procedures, ii) their effects on the structure via post-activation measurement of N_2 adsorption and X-ray diffraction, and iii) the presence of water. The latter can be done via infrared spectroscopy and the use of probe molecules that strongly adsorb on open metal sites, as done in this work. TGA, by itself, on the other hand, is not sufficiently clear and accurate in determining the degassing temperature for these materials. Our TGA results do not show no clear, flat plateaus that match the results of the optimal degassing temperature determined by N_2 adsorption and PXRD, meaning that a poor choice of degassing temperature, resulting in a suboptimal adsorption capacity, is easily made.

That being said, to retain the structure while completely removing water from the open metal sites, cumbersome vacuum procedures are likely needed. Similarly, any streams in contact with the PBAs should be meticulously dry as well due to the highly hydrophilic nature of the materials (Fig. 9). These requirements will potentially limit the use of the open metal sites in PBAs for industrial commercial adsorptive separations. If we focus on the hydrophilic properties, however, then using the PBAs as drying agents, similar to zeolites could be of interest, especially if smaller desiccant volumes and therefore higher densities are required.

5. Conclusion

We performed the first systematic study on the effect of the degassing temperature on the structure, performance, and, in particular, the accessibility of open metal sites using a N_2-based degassing procedure in three distinct PBAs based on the $[Fe(CN)_6]^{3-}$ ion: FePBA, CoPBA, and CuPBA. The activation procedure for each PBA was optimised using a systematic sub-24-h degassing under N_2, allowing us to investigate how degassing temperature influences pore structure, crystal integrity, and, most critically, the activation of open metal sites. Our results indicate that increasing the degassing temperature initially enhances micropore capacity up to an optimal point, beyond which further temperature increases lead to a decrease in microporosity. For CoPBA and CuPBA, this reduction coincides with deterioration of the crystalline structure, whereas the crystallinity of FePBA appears to remain intact, initially. The temperatures corresponding to maximum micropore capacity were found to be 100 °C for FePBA, 100 °C for CoPBA, and 120 °C for CuPBA.

Using these optimised conditions, CO_2 adsorption measurements revealed no strong interactions and DRIFTS analyses after in-situ degassing confirmed that residual water remained in the PBAs. However, CO adsorption demonstrated that a small fraction of open metal sites was accessible, indicating partial activation and likely water-free sites. Consequently, while sub-24-h N_2 flow-based degassing can achieve partial activation, complete activation of the tested PBAs is not attainable under these conditions.

These findings highlight that PBA activation is a non-trivial process. Careful control of degassing conditions is essential to both expose open metal sites and preserve structural integrity, which is critical for gas adsorption applications. In practice, this may necessitate prolonged vacuum degassing to effectively remove moisture and ensure the adsorbent remains dry, as well as reliable methods for assessing

adsorbent dryness. In gas separation applications, such extensive vacuum treatment may pose practical limitations for the use of PBAs. Additionally, to fully exploit open metal sites, the humidity of the adsorption gas must be minimized to prevent competitive adsorption and water retention. Notably, water condenses in the micropores even at low relative humidity, reaching gravimetric adsorption capacities comparable to those of zeolites and volumetric capacities exceeding them. This suggests that microporous PBAs hold significant potential for drying applications, particularly where compact adsorbent volumes are desirable.

CRediT authorship contribution statement

Jelco Albertsma: Writing – review & editing, Writing – original draft, Visualization, Investigation, Formal analysis, Data curation. **Christel I. Koopman:** Writing – review & editing, Investigation. **Eise Draaijer:** Writing – review & editing, Investigation. **Willy Rook:** Writing – review & editing, Formal analysis, Data curation. **David A. Vermaas:** Writing – review & editing, Supervision, Funding acquisition, Conceptualization. **Monique A. van der Veen:** Writing – review & editing, Supervision, Project administration, Funding acquisition, Conceptualization.

Declaration of competing interest

The authors declare that they have no known competing financial interests or personal relationships that could have appeared to influence the work reported in this paper.

Acknowledgements

J.A., C.I.K, D.A.V., and M.A.v.d.V thank the TTW Perspectief programme ReCoVR (P19-20) which is (partly) funded by the Dutch research council (NWO).

Appendix A. Supplementary data

Supplementary data to this article can be found online at https://doi.org/10.1016/j.micromeso.2025.113959.

Data availability

All data used in the paper is freely available through the 4TU data repositorydoi.org.

References

[1] International Energy Agency, CO2 Emissions in 2023, Tech. Rep.. URL https://iea.blob. core.windows.net/assets/33 e2badc-b839-4c18-84ce-f6387b3c008f/CO2Emissionsin2023.pdf.

[2] L. Chancel, Global carbon inequality over 1990–2019, Nat. Sustain. 5 (11) (2022) 931–938, https://doi.org/10.1038/s41893-022-00955-z. URL, https://www.nature.com/articles/s41893-022-00955-z.

[3] Oak Ridge National Laboratory, Materials for separation technologies. Energy and emission reduction opportunities, Tech. Rep. (May 2005), https://doi.org/10.2172/1218755. URL, https://www.osti.gov/servlets/purl/1218755/.

[4] J.G. Bell, M.J. Benham, K.M. Thomas, Adsorption of carbon dioxide, water vapor, nitrogen, and sulfur dioxide on activated carbon for capture from flue gases: competitive adsorption and selectivity aspects, Energy Fuels 35 (9) (2021) 8102–8116, https://doi.org/10.1021/acs.energyfuels.1c00339. URL, https://pubs.acs.org/doi/10.1021/acs.energyfuels.1c00339.

[5] E. Pérez-Botella, S. Valencia, F. Rey, Zeolites in adsorption processes: state of the art and future prospects, Chem. Rev. 122 (24) (2022) 17647–17695, https://doi.org/10.1021/acs.chemrev.2c00140. URL, https://pubs.acs.org/doi/10.1021/acs.chemrev.2c00140.

[6] J.-R. Li, R.J. Kuppler, H.-C. Zhou, Selective gas adsorption and separation in metal–organic frameworks, Chem. Soc. Rev. 38 (5) (2009) 1477, https://doi.org/10.1039/b802426j. URL, https://xlink.rsc.org/?DOI=b802426j.

[7] W.L. Queen, M.R. Hudson, E.D. Bloch, J.A. Mason, M.I. Gonzalez, J.S. Lee, D. Gygi, J.D. Howe, K. Lee, T.A. Darwish, M. James, V.K. Peterson, S.J. Teat, B. Smit, J. B. Neaton, J.R. Long, C.M. Brown, Comprehensive study of carbon dioxide adsorption in the metal–organic frameworks M2(dobdc) (M = Mg, Mn, Fe, Co, Ni, Cu, Zn), Chem. Sci. 5 (12) (2014) 4569–4581, https://doi.org/10.1039/c4sc02064b. URL, https://xlink.rsc.org/?DOI=C4SC02064B.

[8] X. Ma, J. Albertsma, D. Gabriels, R. Horst, S. Polat, C. Snoeks, F. Kapteijn, H. B. Eral, D.A. Vermaas, B. Mei, S. De Beer, M.A. Van Der Veen, Carbon monoxide separation: past, present and future, Chem. Soc. Rev. 52 (11) (2023) 3741–3777, https://doi.org/10.1039/d3cs00147d. URL, https://xlink.rsc.org/?DOI=D3CS00147D.

[9] E. Martínez-Ahumada, M.L. Díaz-Ramírez, M.D.J. Velásquez-Hernández, V. Jancik, I.A. Ibarra, Capture of toxic gases in MOFs: SO2, H2S, NH3 and NOx, Chem. Sci. 12 (20) (2021) 6772–6799, https://doi.org/10.1039/d1sc01609a. URL, https://xlink.rsc.org/?DOI=D1SC01609A.

[10] Y. Xie, R. Lin, B. Chen, Old materials for new functions: recent progress on metal cyanide based porous materials, Adv. Sci. 9 (1) (2022) 2104234, https://doi.org/10.1002/advs.202104234. URL, https://onlinelibrary.wiley.com/doi/101002/advs.202104234.

[11] S. Kjeldgaard, I. Dugulan, A. Mamakhel, M. Wagemaker, B.B. Iversen, A. Bentien, Strategies for synthesis of Prussian blue analogues, R. Soc. Open Sci. 8 (1) (2021) 201779, https://doi.org/10.1098/rsos.201779. URL, https://royalsocietypublishing.org/doi/10.1098/rsos.201779.

[12] A. Ludi, H.U. Güdel, Structural chemistry of polynuclear transition metal cyanides, in: Inorganic Chemistry, Springer-Verlag, Berlin/Heidelberg, 1973, pp. 1–21, https://doi.org/10.1007/BFb0016869, series Title: Structure and Bonding, http://link.springer.com/10.1007/BFb0016869.

[13] M. Verdaguer, A. Bleuzen, V. Marvaud, J. Vaissermann, M. Seuleiman, C. Desplanches, A. Scuiller, C. Train, R. Garde, G. Gelly, C. Lomenech, I. Rosenman, P. Veillet, C. Cartier, F. Villain, Molecules to build solids: high *TC* molecule-based magnets by design and recent revival of cyano complexes chemistry, Coord. Chem. Rev. 190–192 (1999) 1023–1047, https://doi.org/10.1016/S0010-8545(99)00156-3. URL, https://www.sciencedirect.com/science/article/pii/S0010854599001563.

[14] A. Simonov, T. De Baerdemaeker, H.L. Boström, M.L. Ríos Gómez, H.J. Gray, D. Chernyshov, A. Bosak, H.-B. Bürgi, A.L. Goodwin, Hidden diversity of vacancy networks in Prussian blue analogues, Nature 578 (7794) (2020) 256–260, https://doi.org/10.1038/s41586-020-1980-y. URL, https://www.nature.com/articles/s41586-020-1980-y.

[15] Kökçam Demir, A. Goldman, L. Esrafili, M. Gharib, A. Morsali, O. Weingart, C. Janiak, Coordinatively unsaturated metal sites (open metal sites) in metal–organic frameworks: design and applications, Chem. Soc. Rev. 49 (9) (2020) 2751–2798, https://doi.org/10.1039/c9cs00609e. URL, https://xlink.rsc.org/?DOI=C9CS00609E.

[16] Y. Yuan, Z. Zhao, R.F. Lobo, B. Xu, Site diversity and mechanism of metal-exchanged zeolite catalyzed non-oxidative propane dehydrogenation, Adv. Sci. 10 (13) (2023) 2207756, https://doi.org/10.1002/advs.202207756. URL, https://onlinelibrary.wiley.com/doi/10.1002/advs.202207756.

[17] S.S. Kaye, J.R. Long, Hydrogen storage in the dehydrated prussian blue analogues M3[Co(CN)6]2 (M = Mn, Fe, Co, Ni, Cu, Zn), J. Am. Chem. Soc. 127 (18) (2005) 6506–6507, https://doi.org/10.1021/ja051168t. URL, https://pubs.acs.org/doi/10.1021/ja051168t.

[18] L. Reguera, C.P. Krap, J. Balmaseda, E. Reguera, Hydrogen storage in copper prussian blue analogues: evidence of H2 coordination to the copper atom, J. Phys. Chem. C 112 (40) (2008) 15893–15899, https://doi.org/10.1021/jp803714j. URL, https://pubs.acs.org/doi/10.1021/jp803714j.

[19] X. Peng, L. Lin, W. Sun, B. Smit, Water adsorption in metal–organic frameworks with openmetal sites, AIChE J. 61 (2) (2015) 677–687, https://doi.org/10.1002/aic.14707. URL, https://aiche.onlinelibrary.wiley.com/doi/10.1002/aic.14707.

[20] J.N. Hall, P. Bollini, Quantification of open-metal sites in metal–organic frameworks using irreversible water adsorption, Langmuir 36 (5) (2020) 1345–1356, https://doi.org/10.1021/acs.langmuir.9b03581. URL, https://pubs.acs.org/doi/10.1021/acs.langmuir.9b03581.

[21] D. Alezi, J.J. Oppenheim, P.J. Sarver, A. Iliescu, B. Dinakar, M. Dincă, Tunable low–relative humidity and high–capacity water adsorption in a bibenzotriazole metal–organic framework, J. Am. Chem. Soc. 145 (46) (2023) 25233–25241, https://doi.org/10.1021/jacs.3c08335. URL, https://pubs.acs.org/doi/10.1021/jacs.3c08335.

[22] J.J. Oppenheim, M. Dincă, isoreticular curves: a theory of capillary condensation to model water sorption within microporous sorbents, J. Am. Chem. Soc. 146 (30) (2024) 20615–20626, https://doi.org/10.1021/jacs.4c02743. URL, https://pubs.acs.org/doi/10.1021/jacs.4c02743.

[23] A. Rajendran, G.K.H. Shimizu, T.K. Woo, The challenge of water competition in physical adsorption of CO2 by porous solids for carbon capture applications – a short perspective, Adv. Mater. 36 (12) (2024) 2301730, https://doi.org/10.1002/adma.202301730. URL, https://onlinelibrary.wiley.com/doi/abs/10.1002/adma.202301730.

[24] M.R. Hartman, V.K. Peterson, Y. Liu, S.S. Kaye, J.R. Long, Neutron diffraction and neutron vibrational spectroscopy studies of hydrogen adsorption in the prussian blue analogue Cu3[Co(CN)6]2, Chem. Mater. 18 (14) (2006) 3221–3224, https://doi.org/10.1021/cm0608600. URL, https://pubs.acs.org/doi/10.1021/cm0608600.

[25] J. Jiménez-Gallegos, J. Rodríguez-Hernández, H. Yee- Madeira, E. Reguera, Structure of porous copper prussian blue analogues: nature of their high H2 storage capacity, J. Phys. Chem. C 114 (11) (2010) 5043–5048, https://doi.org/10.1021/jp910544j. URL, https://pubs.acs.org/doi/10.1021/jp910544j.

[26] S. Chand Pal, R. Krishna, M.C. Das, Highly scalable acid-base resistant Cu-Prussian blue metal-organic framework for C2H2/C2H4, biogas, and flue gas separations, Chem. Eng. J. 460 (2023) 141795, https://doi.org/10.1016/j.cej.2023.141795. URL, https://linkinghub.elsevier.com/retrieve/pii/S1385894723005260.

[27] A. Takahashi, H. Tanaka, D. Parajuli, T. Nakamura, K. Minami, Y. Sugiyama, Y. Hakuta, S.-i. Ohkoshi, T. Kawamoto, Historical pigment exhibiting ammonia gas capture beyond standard adsorbents with adsorption sites of two kinds, J. Am. Chem. Soc. 138 (20) (2016) 6376–6379, https://doi.org/10.1021/jacs.6b02721. URL, https://pubs.acs.org/doi/10.1021/jacs.6b02721.

[28] Y. Jiang, A. Takahashi, T. Kawamoto, M. Asai, N. Zhang, Z. Lei, Z. Zhang, K. Kojima, K. Imoto, K. Nakagawa, S.-i. Ohkoshi, T. Nakamura, High performance sorption and desorption behaviours at high working temperatures of ammonia gas in a cobalt-substituted Prussian blue analogue, Chem. Commun. 54 (84) (2018) 11961–11964, https://doi.org/10.1039/c8cc06457a. URL, https://xlink.rsc.org/?DOI=C8CC06457A.

[29] L.D. Hansen, W.M. Litchman, G.H. Daub, Turnbull's blue and Prussian blue: KFe (III)[Fe(II)(CN)6], J. Chem. Educ. 46 (1) (1969) 46, https://doi.org/10.1021/ed046p46. URL, https://pubs.acs.org/doi/abs/10.1021/ed046p46.

[30] J. Rouquerol, P. Llewellyn, F. Rouquerol, Is the Bet Equation Applicable to Microporous Adsorbents?, 2007, https://doi.org/10.1016/S0167-2991(07)80008-5. URL, https://linkinghub.elsevier.com/retrieve/pii/S0167299107800085.

[31] J.W.M. Osterrieth, J. Rampersad, D. Madden, N. Rampal, L. Skoric, B. Connolly, M. D. Allendorf, V. Stavila, J.L. Snider, R. Ameloot, J. Marreiros, C. Ania, D. Azevedo, E. Vilarrasa-Garcia, B.F. Santos, X. Bu, Z. Chang, H. Bunzen, N.R. Champness, S. L. Griffin, B. Chen, R. Lin, B. Coasne, S. Cohen, J.C. Moreton, Y.J. Colón, L. Chen, R. Clowes, F. Coudert, Y. Cui, B. Hou, D.M. D'Alessandro, P.W. Doheny, M. Dinca, C. Sun, C. Doonan, M.T. Huxley, J.D. Evans, P. Falcaro, R. Ricco, O. Farha, K. B. Idrees, T. Islamoglu, P. Feng, H. Yang, R.S. Forgan, D. Bara, S. Furukawa, E. Sanchez, J. Gascon, S. Telalovic, S.K. Ghosh, S. Mukherjee, M.R. Hill, M. M. Sadiq, P. Horcajada, P. Salcedo-Abraira, K. Kaneko, R. Kukobat, J. Kenvin, S. Keskin, S. Kitagawa, K. Otake, R.P. Lively, S.J.A. DeWitt, P. Llewellyn, B. V. Lotsch, S.T. Emmerling, A.M. Pütz, C. Martí-Gastaldo, N.M. Padial, J. García-Martínez, N. Linares, D. Maspoch, J.A. Suárez Del Pino, P. Moghadam, R. Oktavian, R.E. Morris, P.S. Wheatley, J. Navarro, C. Petit, D. Danaci, M.J. Rosseinsky, A. P. Katsoulidis, M. Schröder, X. Han, S. Yang, C. Serre, G. Mouchaham, D.S. Sholl, R. Thyagarajan, D. Siderius, R.Q. Snurr, R.B. Goncalves, S. Telfer, S.J. Lee, V. P. Ting, J.L. Rowlandson, T. Uemura, T. Iiyuka, M.A. Van Der Veen, D. Rega, V. Van Speybroeck, S.M.J. Rogge, A. Lamaire, K.S. Walton, L.W. Bingel, S. Wuttke, J. Andreo, O. Yaghi, B. Zhang, C.T. Yavuz, T.S. Nguyen, F. Zamora, C. Montoro, H. Zhou, A. Kirchon, D. FairenJimenez, How reproducible are surface areas calculated from the BET equation? Adv. Mater. 34 (27) (2022) 2201502 https://doi.org/10.1002/adma.202201502. URL, https://onlinelibrary.wiley.com/doi/10.1002/adma.202201502.

[32] H.J. Buser, D. Schwarzenbach, W. Petter, A. Ludi, The crystal structure of Prussian Blue: Fe4[Fe(CN)6]3.xH2O, Inorg. Chem. 16 (11) (1977) 2704–2710, https://doi.org/10.1021/ic50177a008. URL, https://pubs.acs.org/doi/abs/10.1021/ic50177a008.

[33] L. Giraldo, J.C. Moreno-Piraján, Investigating discrepancies in adsorption enthalpy predictions: an analysis of CO2 adsorption on HKUSTs, Sustain. Chem. Environ. 8 (2024) 100161, https://doi.org/10.1016/j.scenv.2024.100161. URL, https://linkinghub.elsevier.com/retrieve/pii/S2949839224001044.

[34] J.H. Choe, H. Kim, C.S. Hong, MOF-74 type variants for CO2 capture, Mater. Chem. Front. 5 (14) (2021) 5172–5185, https://doi.org/10.1039/d1qm00205h. URL, https://xlink.rsc.org/?DOI=D1QM00205H.

[35] E.D. Bloch, M.R. Hudson, J.A. Mason, S. Chavan, V. Crocellà, J.D. Howe, K. Lee, A. L. Dzubak, W.L. Queen, J.M. Zadrozny, S.J. Geier, L.-C. Lin, L. Gagliardi, B. Smit, J. B. Neaton, S. Bordiga, C.M. Brown, J.R. Long, Reversible CO binding enables Tunable CO/H2 and CO/N2 separations in metal–organic frameworks with exposed divalent metal cations, J. Am. Chem. Soc. 136 (30) (2014) 10752–10761, https://doi.org/10.1021/ja505318p. URL, https://pubs.acs.org/doi/10.1021/ja505318p.

[36] E. Reguera, J. Rodríguez-Hernández, A. Champi, J.G. Duque, E. Granado, C. Rettori, Unique coordination of copper in hexacyanometallates, Z. Phys. Chem. 220 (12) (2006) 1609–1619, https://doi.org/10.1524/zpch.2006.220.12.1609. URL, https://www.degruyterbrill.com/document/doi/10.1524/zpch.2006.220.12.1609/html.

[37] L. Liu, S.J. Tan, T. Horikawa, D. Do, D. Nicholson, J. Liu, Water adsorption on carbon - a review, Adv. Colloid Interface Sci. 250 (2017) 64–78, https://doi.org/10.1016/j.cis.2017.10.002. URL, https://linkinghub.elsevier.com/retrieve/pii/S0001868617303354.

[38] M. Tatlier, G. Munz, S.K. Henninger, Relation of water adsorption capacities of zeolites with their structural properties, Microporous Mesoporous Mater. 264 (2018) 70–75, 10.1016/j.micromeso.2017.12.031. URL, https://linkinghub.elsevier.com/retrieve/pii/S1387181117308132.

[39] C. Healy, K.M. Patil, B.H. Wilson, L. Hermanspahn, N.C. Harvey-Reid, B.I. Howard, C. Kleinjan, J. Kolien, F. Payet, S.G. Telfer, P.E. Kruger, T.D. Bennett, The thermal stability of metal-organic frameworks, Coord. Chem. Rev. 419 (2020) 213388, https://doi.org/10.1016/j.ccr.2020.213388. URL, https://www.sciencedirect.com/science/article/pii/S0010854520302836.